# The Faraday Effect

## PHY204 - Project P 9

Clemence Moullet [a], Emma Sampietro [b], and Alexander Sascha Rosenbaum [c]

**Abstract.** The objective of the project was to model the Faraday effect, which is the rotation of the polarization angle of an electromagnetic wave in the presence of an external magnetic field directed along its direction of propagation. We developed a one-dimensional Maxwell solver that employs spatial and temporal discretization along with numerical approximations to simulate the effect. To evaluate the accuracy and consistency of our method, we compared the simulation results with the theoretical predictions. Finally, we explored the applications of the Faraday effect across different fields.

## 1 Introduction

Electromagnetic waves passing through materials with a uniform external magnetic field applied in the direction of propagation undergo a rotation of the angle of their polarization. This is known as the Faraday effect. As suggested by its name, it was first observed in 1845 by Michael Faraday. He made the key observation that the polarization of light was rotated after its propagation through a piece of magnetized glass. His observation was one of the first experimental evidences of the the interaction between electromagnetism and light and was therefore foundational in demonstrating that light is an electromagnetic wave [1].

The Faraday effect has diverse applications. In telecommunications, it optimizes fiber optic communication by controlling light polarization, which can be useful in building technology to measure lightning current [2]. Optical isolators, which are crucial for precision instruments, use the Faraday effect to prevent feedback in laser systems [3]. Magneto-optical storage technology relies on the Faraday effect to influence light polarization based on magnetization, which enables data storage solutions in magneto-optic recordings for high density magnetic data, magnetic field sensors and magneto-electronics [4]. The effect is also used for high-precision magnetic field sensing in scientific and industrial applications, in order to be able to measure large-amplitude, fast-rising currents and magnetic fields. Such methods for measuring currents and magnetic fields involves using the Faraday effect on linearly polarized light propagating in single mode fibers [5]. In astronomy, cosmic magnetism can be studied indirectly by observing synchrotron radiation

[a] e-mail: clemence.moullet@polytechnique.edu
[b] e-mail: emma.sampietro@polytechnique.edu
[c] e-mail: alexander.rosenbaum@polytechnique.edu

as well as the Faraday effect. By observing Faraday Rotation of polarziation in the emission of distant, background objects like galaxies, the nature of the magnetic fields lying between the Earth and those objects can be inferred [6]. Remote sensing benefits from the Faraday effect by monitoring environmental and atmospheric conditions, particularly with the observed Faraday effect through the ionosphere using satellite data, which can also help in topographical mapping [7]. Additionally, in nanotechnology, it leads to the development of materials with enhanced magneto-optical properties, advancing remote-sensors and imaging systems of magnetic fields [8]. In biomedical applications, the Faraday effect can be used to probe intracellular magnetic properties and perform magnetic imaging, revealing the location-specific magnetization dynamics of exogenous magnetic nanoparticles within cells [9]. All of these various important applications makes the Faraday effect a valuable and important phenomenon to investigate and understand.

Our project tackles the Faraday effect first through a theoretical understanding of the physics governing the rotation of the polarization angle of an incident linearly polarized electromagnetic wave. We consider an electron oscillating under the effect of this wave, in addition to a constant external magnetic field within the framework of the classical Lorenz model. Using Maxwell's equations, we derive the current density which allows us in turn to find the propagation equation governing the wave in the presence of the external magnetic field. Since any linearly polarized plane wave can be written as the superposition of a left-handed and right-handed circular polarization, we can decompose and then recombine their equations to find the rotation in linear polarization of the initial plane wave, using the difference in phase velocities for each circularly polarized wave. This reveals finally that the rotation in polarization angle of the incident wave has a linear dependence on $L$, the distance for which the wave propagates in the external magnetic field, $B_0$, the external magnetic field, and $V$, the Verdet constant ie. the rotation angle $\beta = VB_0L$. This derivation can similarly be looked at within the framework of indices of refraction, from which we also conclude that varying phase velocities of the different handed circular polarization leads to a rotation of polarization angle.

Following our theoretical understanding, we programmed a 1-dimensional Maxwell solver in python. This program uses Maxwell's equations and the time-evolution of the current density in order to model the propagation of a Gaussian-wavepacket in the presence of a constant external magnetic field to demonstrate the rotation in polarization angle. By discretizing the continuous time and space domains, and using the Finite Difference Time Domain (FDTD) method [10] we were able to approximate partial differential equations with the value of the functions at the previous and current time and space steps, which is crucial to solving Maxwell's equations. Throughout the project a few resources were particularly invaluable that we consulted to improve our understanding of FDTD simulation, including the lecture of EM Possible entitled "Formulation of One-Dimensional FDTD" [11], as well as the textbook "Understanding the Finite-Difference Time-Domain Method" by John B. Schneider [10]. We also thank Professor Couairon for his help in programming, and for the resources he provided.

Finally we investigate a few of the specific applications of the Faraday effect, including in the effect in plasmonic and magnetic materials, its application to measuring lightning current and in fiber-optic sensors, as well as in the ionosphere and satellite topographical modeling. At the culmination of this project, we effectively modeled the Faraday effect, in demonstrating a rotation angle in polarization of a simulated wave, and the theoretical derivation of this angle.

## 2 Theoretical background

We consider a Lorentz model for an electron carrying charge $-e = -1.6 \times 10^{-19}C$ with mass $m_e = 9.1 \times 10^{-31}$kg, moving at speed $\vec{v_e}$, which oscillates due to the propagation of an electromagnetic wave, in the presence of an external constant magnetic field $\vec{B_0}$, directed in its direction of propagation.
The differential equation satisfied by the position of the electron is:

$$\ddot{\vec{\underline{r}}} + \gamma \dot{\vec{\underline{r}}} + \omega_0^2 \vec{\underline{r}} = \frac{-e}{m_e}(\vec{E} + \vec{v_e} \times \vec{B}) + \frac{-e}{m_e}\vec{v_e} \times \vec{B_0}$$

where $\gamma = \frac{1}{\tau}$ is the damping rate, with $\tau$ the collision time in the medium, and $\omega_0^2 = \frac{e^2}{4\pi\epsilon_0 m_e R^3}$ with $R = 1$Å the radius of the atom.
Since, in the case of non relativistic motion ($|\vec{v_e}| \ll c$), for infinite plane waves, we have $|\vec{v_e} \times \vec{B}| = |\vec{v_e} \times \frac{\vec{k} \times \vec{E}}{\omega}| \approx |\frac{\vec{v_e}}{c}\vec{E}| \ll |\vec{E}|$, we neglect the contribution given by the $\vec{B}$ field, giving

$$\ddot{\vec{\underline{r}}} + \gamma \dot{\vec{\underline{r}}} + \omega_0^2 \vec{\underline{r}} = \frac{-e}{m_e}\vec{E} + \frac{-e}{m_e}\vec{v_e} \times \vec{B_0}$$

By considering:

- An electromagnetic plane wave, of frequency $\omega$ propagating in the $x$ direction ($E_x = 0$). This choice is useful as any electromagnetic wave can be decomposed as a superposition of plane waves.
- The external magnetic field along the direction of propagation of the wave $\vec{B_0} = B_0\vec{e_x}$
- The collision time is $\tau$ is large enough to neglect the contribution of the $\gamma\dot{\vec{\underline{r}}}$ with respect to the other terms in the equation

and solving the differential equation for the position with an ansatz as introduced in Appendix A.1, we derive the current density, where we have used the cyclotron frequency $\Omega = \frac{eB_0}{m_e}$ and the plasma frequency satisfying $\omega_p^2 = \frac{ne^2}{m_{e0}}$, with $n$ the electron density.

$$\vec{j} = \begin{pmatrix} j_y \\ j_z \end{pmatrix} = -ne\vec{v} = \frac{-i\omega\omega_p^2\epsilon_0}{(\omega_0^2 - \omega^2)^2 - (\omega\Omega)^2)} \begin{pmatrix} \omega_0^2 - \omega^2 & i\omega\Omega \\ -i\omega\Omega & \omega_0^2 - \omega^2 \end{pmatrix} \begin{pmatrix} E_y \\ E_z \end{pmatrix} =: [\sigma] \begin{pmatrix} E_y \\ E_z \end{pmatrix} \tag{1}$$

Using Maxwell's equations (see Appendix A.1) we find the two dispersion relations, respectively satisfied for right-handed (of the form $\begin{pmatrix} E_y \\ -iE_z \end{pmatrix}$) and left-handed circular polarizations ($\begin{pmatrix} E_y \\ iE_z \end{pmatrix}$):

$$\begin{cases} k_R^2 = \frac{\omega^2}{c^2}(1 + \frac{\omega_p^2}{(\omega_0^2 - \omega^2) - (\omega\Omega)}) \\ k_L^2 = \frac{\omega^2}{c^2}(1 + \frac{\omega_p^2}{(\omega_0^2 - \omega^2) + (\omega\Omega)}) \end{cases}$$

and the corresponding phase velocities

$$\begin{cases} v_R = \dfrac{c}{\sqrt{1+\frac{\omega_p^2}{(\omega_0^2-\omega^2)-(\omega\Omega)}}} \\ v_L = \dfrac{c}{\sqrt{1+\frac{\omega_p^2}{(\omega_0^2-\omega^2)+(\omega\Omega)}}} \end{cases}$$

In other words, right-handed circularly polarized wave propagate at velocity $v_R$ in the medium while left-handed circularly polarized wave propagate at velocity $v_L$. Furthermore, from this derivation, we directly identify the index of refraction $n_R^2 = 1 + \frac{\omega_p^2}{(\omega_0^2-\omega^2)-(\omega\Omega)}$ and $n_L^2 = 1 + \frac{\omega_p^2}{(\omega_0^2-\omega^2)+(\omega\Omega)}$. This reveals the circular birefringence of the medium due to the external magnetic field.

Since we can write any linearly polarized plane wave as the superposition of a left-handed and right-handed circular polarization, we can decompose and then recombine their equations to find the rotation in linear polarization of the initial plane wave.

We recall that we were initially considering a $y$-polarized electromagnetic wave, propagating in the positive $x$-direction (to simplify the discussion, we consider the initial phase to be 0, but our reasoning can easily be applied with a non-zero phase):

$$\vec{E} = E_0 \cos(kx - \omega t)\vec{e_y}$$

or equivalently:

$$\vec{E} = \frac{1}{2}E_0((\cos(kx-\omega t)\vec{e_y} + \sin(kx-\omega t)\vec{e_z} + (\cos(kx-\omega t)\vec{e_y} - \sin(kx-\omega t)\vec{e_z}))$$

where the first and second parenthesis can respectively be identified as a right-handed and left-handed circular polarized wave.
Then, after propagating through a medium of length $L$, due to the Faraday effect, we now have:

$$\vec{E}(x=L) = \frac{1}{2}E_0((\cos(k_R L-\omega t)\vec{e_y} + \sin(k_R L-\omega t)\vec{e_z} + (\cos(k_L L-\omega t)\vec{e_y} - \sin(k_L L-\omega t)\vec{e_z}))$$

and we have identified $k_1 = k_R$ and $k_2 = k_L$. Using trigonometric identities, the field can be rewritten as:

$$\vec{E}(x=L) = E_0(\cos(\frac{k_R+k_L}{2}L - \omega t)(\cos(\frac{k_R-k_L}{2}L)\vec{e_y} + \sin(\frac{k_R-k_L}{2}L)\vec{e_z})$$

We identify as the rotation angle $\beta$:

$$\beta = \frac{k_R - k_L}{2}L$$

We now consider that $\omega$ is far enough from resonance such that $\frac{\omega\Omega}{\omega_0^2-\omega^2}$. As detailed in Appendix A.2, we use a Taylor expansion and find that

$$\beta = VB_0L \tag{2}$$

where $V$ is called the Verdet constant and is identified as $V = \frac{k_R^2-k_L^2}{k_R+k_L} = \frac{\omega^2 e}{2m_e c}\frac{\omega_p^2}{(\omega_0^2-\omega^2)^2(1+\frac{\omega_p^2}{\omega_0^2-\omega^2})^{\frac{1}{2}}}$

Under the assumption that $\omega_0 \approx 0$, as it is the case in a plasmonic material, and as we will consider for our simulation in section 3, and considering $\omega_p \ll \omega$, we can further simplify the expression of $V$: $V = \frac{e}{2m_e c}\frac{\omega_p^2}{\omega^2}$.

The Verdet constant is material dependent, the Faraday rotation being linked to how dispersive the medium is. For example light flint glass has a high Verdet constant (at 20°, for $\lambda = 578nm$, $V = 0.0317$ min of arc.gauss$^{-1}$.cm$^{-1}$), while air has a very low Verdet constant (at a pressure of 760 mm Hg, for $\lambda = 578nm$, at 0° $V = 6.27e^{-6}$ min of arc.gauss$^{-1}$.cm$^{-1}$)[12].

### 2.1 The Faraday Effect, a qualitative approach via the index of refraction

Our derivations in the previous section show that the Faraday effect results of the dependence of the current $\vec{j}$ depending on the handedness of the circular polarization, leading to a difference in the index of refraction for a right-handed and left-handed circular polarized wave. This birefringence can also be understood by directly considering the frequency dependence of the index of refraction for a wave propagating in a medium.

We model the atoms in the medium as magnetic dipoles and make the following important assumption: we consider that we work with an incident wave away from the resonant frequency of electrons and therefore neglect their quantum behavior (spin contribution in the magnetic momentum). As a result, the giromagnetic ratio is $\gamma = \frac{-e}{2m}$ and, due to the external $\vec{B}$ field the electrons rotate about the $x$ axis, anticlockwise, at the Larmor frequency $\omega_L = -\gamma B_0 = \frac{eB_0}{2m_e}$, (anticlockwise rotation)[1].

As a result, in the frame of reference of the oscillating electrons, the right-handed circular component (clockwise rotation in time) of the linearly polarized wave is seen to oscillate at a frequency $\omega + \omega_L$, while the left-handed circular component appears to be oscillating at the frequency $\omega - \omega_L$.

Since we are away from the absorption frequency for the electrons of the atom, the index of refraction $n$ is real and we recall that, in the absence of an external magnetic field, it verifies $n(\omega) = 1 + \frac{n_e^2}{2m_e\epsilon_0}\frac{1}{\omega_0^2 - \omega^2}$ with $\omega$ the frequency of the wave, as indicated in figure 1. The difference in frequency of the two circular polarized components of the incident wave, as seen in the frame of reference of the electrons, then explains the difference in index in refraction.

As shown in the previous section, we retrieve that the right-handed circular component has higher index of refraction (slower phase velocity) then the left-handed circular component.

[1] The reader is invited to consult PHY204 textbook Chapter 9 *Magnetic media - Paramagnetism, diamagnetism, ferromagnetism*, section 9.3.1 *The Larmor precession* for the details of this derivation

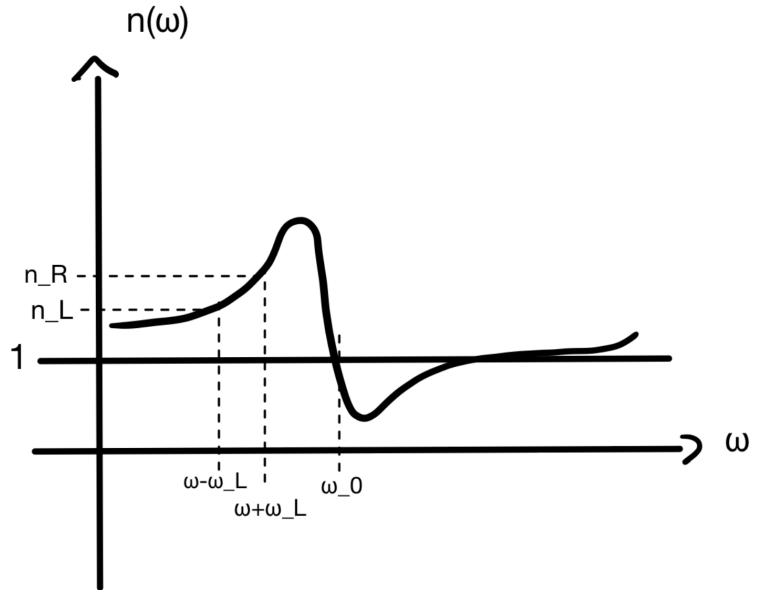


Fig. 1: Qualitative representation of the refractive index as a function of $\omega$ for a resonance frequency $\omega_0$ in the UV[12], . From the previous derivation: the index of refraction for the right-handed circular polarization is $(1+\frac{\omega_p^2}{(\omega_0^2-\omega^2)-(\omega\Omega)})^{\frac{1}{2}}$ and for the left-handed circular polarization $n_L = (1+\frac{\omega_p^2}{(\omega_0^2-\omega^2)+(\omega\Omega)})^{\frac{1}{2}}$

## 3 Simulation method

To be able to simulate the propagation of a wavepacket in a medium, we used Maxwell's equations and the time evolution of the current density. We performed numerical approximations according to the Finite difference time derivative (FDTD) method, where we discretized the time and space domain and performed some approximations for the simulation.

### 3.1 Model of the simulation

In our simulation, we consider a Gaussian pulse, propagating in the $x$ direction. The $\vec{E}$ field is polarized along the $y$ direction. We model a medium where the damping time $\tau$ is large enough to consider the motion of the electrons to be undamped. Furthermore, we reduce our model to a medium where electrons have no resonant frequency ($\omega_0 \approx 0$). This assumption (which holds in plasmonic media) still allows to capture the Faraday effect and greatly simplifies the model.

Time and space evolution of the electric and magnetic fields and of the current term are solved using FDTD in a staggered Yee-grid layout [10]. In this grid, electric and magnetic fields are offset by half a grid cell. The current is computed at the same point as the magnetic field as represented in Figure 2. Note that, in practice, the implementation of the scheme in Python then requires to convert the half-indices to full integer values: the electric and magnetic field components are then separated by 1 full grid cell.

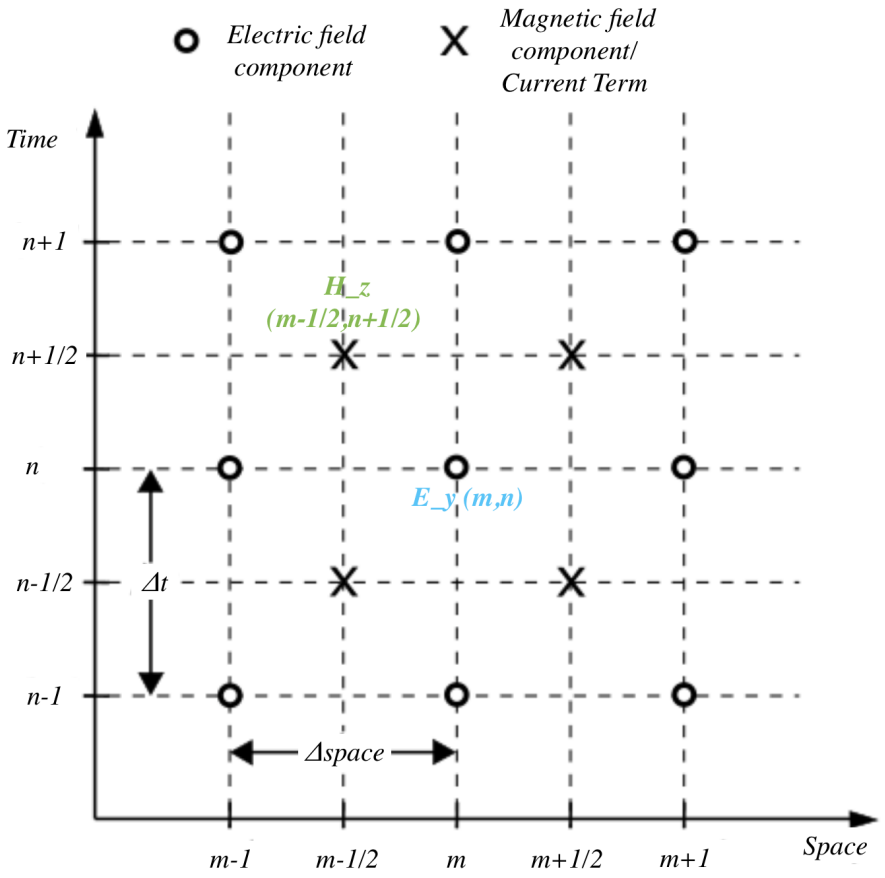


Fig. 2: Representation of the Yee-staggered grid [13]

### 3.2 Time evolution of the current term

We recall that, using Newton's equation for the motion of a bound electron (1) multiplied by $-ne$, neglecting the $\omega_0$ term by assuming we are in a plasma, we find the time evolution differential equation of the current density $\vec{J}$:

$$\frac{\partial \vec{J}}{\partial t} = -\gamma \vec{J} + \frac{ne^2}{m}\vec{E} - \frac{e}{m}\vec{J} \times \vec{B}_0$$

By projecting $\vec{J}$ along the $y$ and $z$ axes, setting $\omega_c = \frac{eB_0}{m}$ and $\omega_p^2 = \frac{ne^2}{\epsilon_0 m}$ we have:

along the $y$-axis:

$$\frac{\partial J_y}{\partial t} + \gamma J_y + \omega_c J_z = \epsilon_0 \omega_p^2 E_y \tag{3}$$

along the $z$-axis:

$$\frac{\partial J_z}{\partial t} + \gamma J_z - \omega_c J_y = \epsilon_0 \omega_p^2 E_z \tag{4}$$

We will compute a semi-analytical solution for these coupled equations, letting $J_+ = J_y + iJ_z$. By taking equation 3+i4, we find:

$$\frac{\partial J_+}{\partial t} + \gamma J_+ - i\omega_c J_+ = \epsilon_0 \omega_p^2 (E_y + iE_z) \tag{5}$$

Setting $\Gamma = \gamma - i\omega_c$, we obtain the equation:

$$\frac{\partial J_+}{\partial t} + \Gamma J_+ = \epsilon_0 \omega_p^2 (E_y + iE_z) \tag{6}$$

The solution A.3 is:

$$J_+(t) = J_+(t_0)e^{-\Gamma(t-t_0)} + \epsilon_0\omega_p^2 \int_{t_0}^{t} e^{\Gamma(t'-t)}[E_y(t') + iE_z(t')]dt'$$

We integrate over a step $\Delta t$ (considering $t_0$ to be at $t - \frac{1}{2}$ and $t$ at $t + \frac{1}{2}$), and evaluating the integrand at the midpoint $t$ (rectangle law), we get
$J_+(t + \Delta t/2) = J_+(t - \Delta t/2)e^{-\Gamma \Delta t} + \Delta t \epsilon_0 \omega_p^2 [E_y(t) + iE_z(t)]$

By taking real and imaginary parts of $J_+$, we reconstruct $J_y$ and $J_z$:

$$J_y(t + \Delta t/2) = [J_y(t - \Delta t/2)\cos(\omega_c \Delta t) - J_z(t - \Delta t/2)\sin(\omega_c \Delta t)]e^{-\gamma \Delta t} + \Delta t \epsilon_0 \omega_p^2 E_y(t) \tag{7}$$

$$J_z(t + \Delta t/2) = [J_y(t - \Delta t/2)\sin(\omega_c \Delta t) + J_z(t - \Delta t/2)\cos(\omega_c \Delta t)]e^{-\gamma \Delta t} + \Delta t \epsilon_0 \omega_p^2 E_z(t) \tag{8}$$

### 3.3 Time evolution of the fields

We recall $\vec{H} = \frac{\vec{B}}{\mu_0} - \vec{M} = \frac{\vec{B}}{\mu_0}$ since we consider no magnetization ie. $\vec{M} = 0$.
We recall Maxwell's equations:

- $\nabla \times \vec{E} = -\mu_0 \frac{\partial \vec{H}}{\partial t}$
- $\nabla \times \vec{H} = \vec{J} + \epsilon_0 \frac{\partial \vec{E}}{\partial t}$

We performed numerical approximations according to the **FDTD** method which allows to approximate partial differential equations with the value of the functions at the previous and current time/space step, so that for all components $i = y, z$ and fields $F = H, E$:

- $\frac{\partial F_i}{\partial x}\big|_{x+\frac{\Delta x}{2}} \approx \frac{F_i(x+\Delta x) - F_i(x)}{\Delta x}$
- $\frac{\partial F_i}{\partial t}\big|_{t+\frac{\Delta t}{2}} \approx \frac{F_i(t+\Delta t) - F_i(t)}{\Delta t}$

Moreover, we **discretize the time domain** to transform the equations into a simpler form (using the staggered grid/Yee-grid, [10]) as introduced in section 3.1. In our code, we set $m$ the iteration index for $x$, $n$ the index for time.

This gives us:

- $\frac{E_y(m+1,n) - E_y(m,n)}{\Delta x} \approx \mu_0 \frac{H_z(m+\frac{1}{2}, n+\frac{1}{2}) - H_z(m+\frac{1}{2}, n-\frac{1}{2})}{\Delta t}$
- $\frac{H_z(m+\frac{1}{2}, n+\frac{1}{2}) - H_z(m-\frac{1}{2}, n+\frac{1}{2})}{\Delta x} \approx (J_y(n+\frac{1}{2}) + \epsilon_0 \frac{E_y(m,n+1) - E_y(m,n)}{\Delta t})$

For the sake of Python implementation, we change our variables to integer indices so that we can iterate over a loop. The magnetic/current terms are now separated by 1 grid cell from the associated electric field component and we shift indices in the following way: $\frac{1}{2} \mapsto +1$ and $\frac{-1}{2} \mapsto -1$. To respect

the the staggered grid structure, for the magnetic field and current the space indices range from 0 to $m_{max}-1$, while for the electric field, the space indices range from 1 to $m_{max}$. We can find the ($E_y$,$H_z$) at time $t$ (=$n$) and position $x$ (=$m$) from their values at the previous space and time steps:

- $H_z(m,n) = H_z(m,n-1) + \frac{\Delta t}{\mu_0 \Delta x}(E_y(m+1,n) - E_y(m,n))$
- $E_y(m,n+1) = E_y(m,n) + \frac{\Delta t}{\epsilon_0 \Delta x}(H_z(m+1,n) - H_z(m,n)) - \frac{\Delta t}{\epsilon_0} J_y(n)$

Similarly, the couple ($E_z$,$H_y$) satisfies:

- $H_y(m,n) = H_y(m,n-1) + \frac{\Delta t}{\mu_0 \Delta x}(E_z(m+1,n) - E_z(m,n))$
- $E_z(m,n+1) = E_z(m,n) + \frac{\Delta t}{\epsilon_0 \Delta x}(H_y(m+1,n) - H_y(m,n)) - \frac{\Delta t}{\epsilon_0} J_z(n)$

We introduce the "Courant number" $S_c = \frac{c\Delta t}{\Delta x}$, vacuum impedance $Z_0 = \sqrt{\mu_0/\epsilon_0}$ as well as the cyclotron frequency $\omega_c = \frac{eB_0}{m}$ and the plasma frequency $\omega_p^2 = \frac{ne^2}{\epsilon_0 m}$. Moreover, we normalize the current density: $\tilde{J} = J/(\Delta t \epsilon_0 \omega_p^2)$ to minimize the constants appearing in the scheme. This gives us the equations to update the electric and magnetic fields, together with the update of the current J from 7 and 8:

- $H_z(m,n) = H_z(m,n-1) + \frac{S_c}{Z_0}(E_y(m+1,n) - E_y(m,n))$
- $H_y(m,n) = H_y(m,n-1) + \frac{S_c}{Z_0}(E_z(m+1,n) - E_z(m,n))$

- $\tilde{J}_y(m,n) = [\tilde{J}_y(m,n-1)\cos(\omega_c \Delta t) - \tilde{J}_z(m,n-1)\sin(\omega_c \Delta t)]e^{-\gamma \Delta t} + E_y(m,n)$
- $\tilde{J}_z(m,n) = [\tilde{J}_y(m,n-1)\sin(\omega_c \Delta t) + \tilde{J}_z(m,n-1)\cos(\omega_c \Delta t)]e^{-\gamma \Delta t} + E_z(m,n)$

- $E_y(m,n+1) = E_y(m,n) + Z_0 S_c(H_z(m+1,n) - H_z(m,n)) - (\omega_p \Delta t)^2 \tilde{J}_y(m,n)$
- $E_z(m,n+1) = E_z(m,n) + Z_0 S_c(H_y(m+1,n) - H_y(m,n)) - (\omega_p \Delta t)^2 \tilde{J}_z(m,n)$

We recall the formula for the impedance $Z = \frac{|\vec{E}|}{|\vec{H}|}$. Since for infinite plane waves in vacuum, $\vec{H} = \frac{\vec{B}}{\mu_0} = \frac{\vec{k}\times\vec{E}}{\omega\mu_0}$, then $|\vec{H}| = \frac{|\vec{E}|}{c\mu_0}$. Finally we find the free space impedance $Z_0 = \sqrt{\frac{\mu_0}{\epsilon_0}} \approx 377\Omega$.

Then, in order to have $\vec{E}$ and $\vec{H}$ of the same order of magnitude, we will use $\vec{H}' = \vec{H} Z_0$ in the code [14], reason why we set $Z_0 = 1$ (relative to the scheme above) as one of the constants.

We choose $dx = 25e-9$ and $dt = 0.9 * dx/c$. We choose the time step such that it satisfies the Courant condition $\Delta t \leq \frac{\Delta x}{c}$

### 3.4 Defining the boundary conditions

In order to avoid reflection at the boundaries of our medium, we implement the Absorbing Boundary condition (ABC)[10]:

$$E_y(m=0,n+1) = E_y(m=1,n)$$

$$H_z(m_{max},n) = H_z(m_{max}-1,n-1)$$

We impose the analogous condition for the couple ($E_z$, $H_y$) Note that this absorbing boundary conditions is designed for the Courant number $S_c = c * \frac{dt}{dx} = 1$ by ensuring that the wave propagation equation in

vacuum is satisfied for the left-propagating and right-propagating waves. Although we do not have $S_c = 1$ in our simulation, the implementation of this Absorbing Boundary Condition operates well enough for us to avoid most reflection and to obtain a satisfactory model.

### 3.5 Introducing the source and defining constants

We choose a **gaussian wavepacket** as a wave source. We consider a **wave propagating in the $x$-direction with the electric field being polarized along the y axis** initially (meaning $E_x = E_z = 0$, initially). We introduce both the electric and the magnetic field at the space step at which we define the source ($m_{source}$ in our code) as:

- $\vec{E_s}(t) = \exp(-\frac{(t-t_0)^2}{\tau^2}) \sin(\omega_0 t)\vec{e_y}$
- $\vec{B_s}(t) = \frac{1}{c} \exp(-\frac{(t-t_0)^2}{\tau^2}) \sin(\omega_0 t)\vec{e_z}$ [2]

where $\omega_0 = \frac{2\pi c}{\lambda_0}$.
We indicate below the main constants and numerical values taken in our simulation:

| **Physical Quantity** | **Numerical value** |
|---|---|
| Electron mass $m_e$ | $9.1 \times 10^{-31}$ kg |
| Elementary charge $q_e$ | $1.6 \times 10^{-19}$ C |
| Electron number density $n$ | $1 \times 10^{27}\mathrm{m}^{-3}$ |
| Damping rate $\gamma$ | $1\mathrm{s}^{-1}$ |
| External magnetic field value $B_0$ | 500 T |
| Wavelength of the source $\lambda_{\text{source}}$ | 550 nm |
| Parameters of the source: $\tau$ and $t_0$ | $\tau = 10$ fs and $t_0 = 2\tau$ |
| Index for the start of the source $m_{source}$ | 1 |
| Space step $dx$ | 25 nm |
| Time step $dt$ | $0.9dx/c$ s |

Table 1: Summary of the main values taken for our numerical simulation. **Note that we set the magnetic field $B_0$ deliberately high to compensate for the short propagation length $L$ of the pulse through the medium (necessary for runtime concerns). Indeed we recall that the rotation angle $\beta$, which we aim to capture, is proportional to $B_0 L$*

## 4 Results and Discussion

From our numerical simulation of the effect, with a Gaussian wavepacket initially polarized along the $y$-axis, we observe a gradual decrease in the $y$ component of the magnetic field coupled with a gradual increase in its $z$ component.

[2] The associated $\vec{B}$ field is computed from the formula $\vec{B} = \frac{\vec{k}\times\vec{E}}{\omega}$, valid for plane waves and for a Gaussian pulse, as a superposition of plane waves

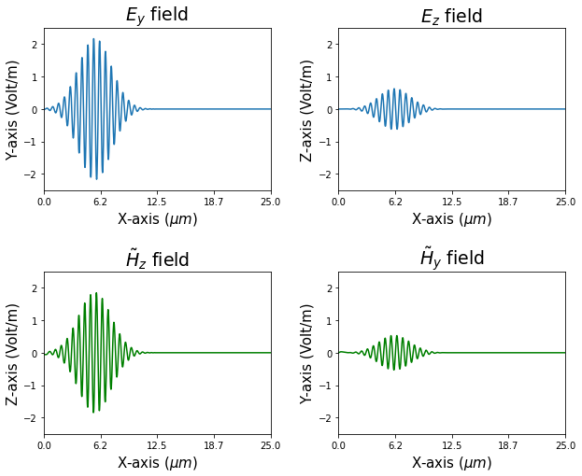


Fig. 3: Wavepacket entering the medium

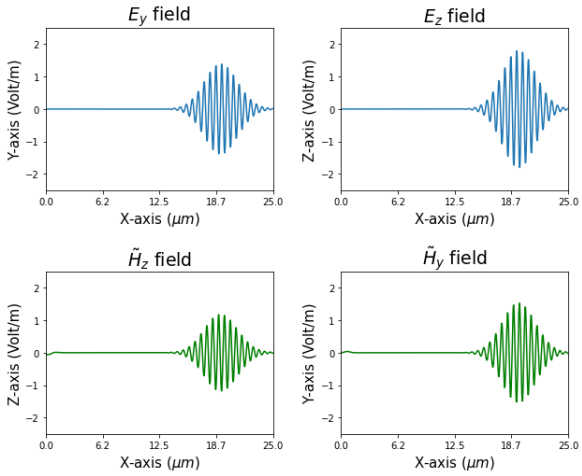


Fig. 4: Wavepacket after travelling through medium

Fig. 5: Rotation in polarization seen from the fields projections along the axis for $B_0 = 500$T

This result demonstrates a rotation of polarization of the Gaussian-wave packet. Moreover, by adding diagnostics to our code, we were able to extract the polarization angle at each time step (Figure 6) and then extract the final angle of rotation of polarization. We can observe that, while most of the curve 6 is linear, in accordance to our theoretical expectation, the first part of the graph is not perfectly linear. This is due to the fact that the wavepacket has not fully entered the material yet, which influences our diagnostic of the angle, which takes the tangent of the ratio of the maximal components of the electric field.

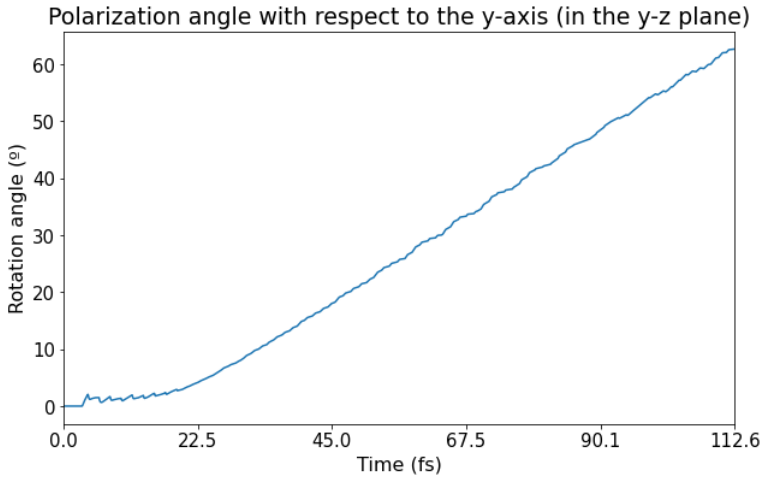


Fig. 6: Polarization angle in function of time as the wave propagates through the medium for $B_0 = 500$T and $L = 28.7\mu$m

We observed a linear increase in the angle of rotation of polarization when the propagation distance (number of space steps) was increased, which is what we expect to see from the theoretical expression of

the rotation angle 2. In the table and in Figure 7, we present a few values for the propagation distance performed in the simulation, and the final rotation angle to demonstrate this linear response.

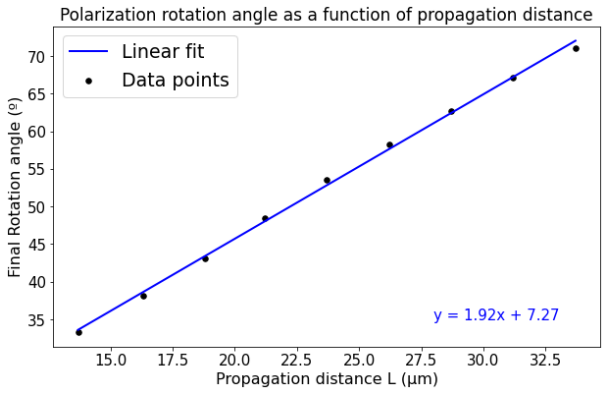


(a) Linear dependency of the polarization angle with respect to the propagation distance

| Propagation distance ($\mu$m) | Final Rotation angle (º) |
|---|---|
| 13.7 | 33.3º |
| 16.3 | 38.1º |
| 18.8 | 43.1º |
| 21.2 | 48.4º |
| 23.7 | 53.6º |
| 26.2 | 58.3º |
| 28.7 | 62.7º |
| 31.2 | 67.1º |
| 33.7 | 71.1º |

(b) Table with our simulation results

Fig. 7: Dependence on the polarization angle on the propagation length for fixed $B_0 = 500$T

Similarly, we tested the dependence of the rotation angle in our simulation on the magnitude of the magnetic field, fixing the propagation length. Again, we observed a linear dependence which is in accordance with our theoretical derivations, as can be seen from the table and Figure 8.

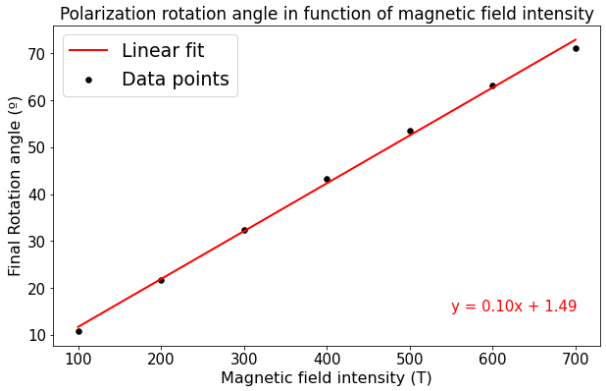


(a) Linear dependency of the polarization angle with respect to the intensity of the external magnetic field

| Magnetic field (T) | Final Rotation angle (º) |
|---|---|
| $1 \times 10^2$ | 10.8º |
| $2 \times 10^2$ | 21.6º |
| $3 \times 10^2$ | 32.4º |
| $4 \times 10^2$ | 43.2º |
| $5 \times 10^2$ | 53.6º |
| $6 \times 10^2$ | 63.2º |
| $7 \times 10^2$ | 71.2º |

(b) Table with our simulation results

Fig. 8: Dependence on the polarization angle on the magnetic field intensity for fixed length $L = 23.7\mu$m (950 space steps)

We then compared the slopes of the curves of our simulations with the respective theoretical values. By performing a linear fit of our simulated angles in function of the propagation distance 7, we find the slope of the curve to be $\alpha = 1.92 \times 10^6 \text{m}^{-1}$ which is consistent with the theoretical value deduced from

2 using $V = 70.36\mathrm{T}^{-1}\,\mathrm{m}^{-1}$ 9 of

$$VB = 70.36\mathrm{T}^{-1}\,\mathrm{m}^{-1} \times 500\mathrm{T} = 35177.58\ \mathrm{rad}\ \mathrm{m}^{-1} = 2.02 \times 10^{6}\ \mathrm{deg}\ \mathrm{m}^{-1}$$

By performing a linear fit of our simulated angles in function of the magnetic field intensity 8, we find the slope of the curve to be $\alpha = 0.10\ \mathrm{degT}^{-1}$ which is consistent with the theoretical value, deduced from 2 using $V = 70.36\mathrm{T}^{-1}\,\mathrm{m}^{-1}$ 9 of

$$VL = 70.36\mathrm{T}^{-1}\,\mathrm{m}^{-1} \times 23.7\mu\mathrm{m} = 0.0017\ \mathrm{radT}^{-1} = 0.096\ \mathrm{degT}^{-1}$$

Therefore, we can conclude that our simulations not only respect the linear behaviours of the theoretical equations but also give a consistent quantitative result.

In both cases above to compute the Verdet constant, we used $\omega = \frac{2\pi c}{\lambda} = \frac{2\pi c}{550\mathrm{nm}} = 3.43 \times 10^{15}\mathrm{s}^{-1}$ and taking $n = 10^{27}\mathrm{m}^{-2}$, we have $\omega_p = (\frac{ne^2}{m\epsilon_0})^{\frac{1}{2}} = 1.78 \times 10^{15}\mathrm{s}^{-1}$ and so

$$V = \frac{e}{2m_e c}\frac{\omega_p^2}{\omega^2} = 70.36\mathrm{T}^{-1}\,\mathrm{m}^{-1} \tag{9}$$

Values of this magnitude for the Verdet constant would be considered high but reasonable, making it a good material for magneto-optical applications. In fact, materials such as the Terbium-doped glass have values of the Verdet constant in this range (varying depending on wavelength, temperature and other factors) [15]. Terbium-doped glasses are glasses containing small amounts of terbium ions incorporated into the glass matrix. Terbium is an element with unpaired electrons that has strong magnetic moments. Terbium-doped glasses are therefore used in devices involving Faraday rotation, such as optical insulators in fiber optic communication systems 5.1.

# 5 Applications of the Faraday effect

## 5.1 The Faraday effect for fiber-optic sensors: a technology to measure lightning current

The rotation of the incident field induced by the Faraday Effect can be related to the external magnetic field through the Verdet proportionality constant $V$:

$$\beta = V \int \boldsymbol{B} d\boldsymbol{l}$$

From Ampère's law, the rotation angle can then be linked to the current circulating through a closed loop $l$:

$$\beta = V \mu_0 I$$

This proportionality is the basis of technologies using optical fibers to measure current. We will provide an overview of the functioning principle of Fiber Optics Current Sensors (FOCS), their advantages and disadvantages, and discuss an application for measuring lightening current, for example, during plane flights, based on the paper *Lightning Current Measurement with Fiber-Optics Sensor* by T. X. Nguyen et al [2].

### 5.1.1 Fiber Optics Current Sensors

Using the superposition principle for Ampère's law, we find that an N fiber coil looped around a conductor would yield the relation:

$$\beta = V \mu_0 N I$$

We recall that the only observable that can be measured for light is the power. In order to indirectly measure the Faraday rotation angle, one can use a polarimetric detection scheme, the most common being the dual-quadrature polarimetric detection scheme as detailed in Figure 9. Incident light is linearly polarized by an initial polarizer. As it travels through the optical fibers looped around the conductor, the light is submitted to the Faraday effect and its polarization shifted by an angle $\beta$. Finally, the Wollaston prism splits the output beam in two orthogonally polarized beams which are detected by two separate photo diodes. An analog circuit computes the output function: $S = \frac{I_1 - I_2}{I_1 + I_2}$. We find $S = \sin(2\beta)$ (detail in the appendix). The current in the sensing element is then recovered as:

$$I_c = \frac{sin^{-1}(S)}{2\mu_0 V N L}$$

From this formula, we notice that an increased number of fiber loops or a longer optical path can improve the sensitivity of the measurement.

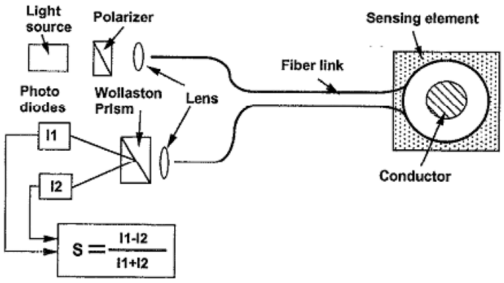


Fig. 9: Dual quadrature polarimetric detection scheme [16]

### 5.1.2 Advantages and disadvantages

The advantages of using optical fibers for current sensing include:

- absence of saturation effects: optical fibers are typically built with silica-based materials, where the Verdet constant is small, leading to a small rotation angle in spite of a large magnetic field
- immunity to electromagnetic interferences
- non-intrusive and non-conductive device
- sensitivity can be modulated by changing the number of loops N
- lightweight, versatile and small

On the other hand, disadvantages include:

- temperature dependence: one should note that the Verdet constant of a Faraday material and the optical path in a optical fiber both depend on the temperature. Furthermore, the optical properties of the elements used in the polarimetric detection scheme might also be affected by a temperature change.
- bends and vibrations in the optical fiber might induce a change in polarization, not due to the Faraday effect, that would offset the measured value of current. [16]

### 5.1.3 Application to measurement of lightning current on planes

The flexibility and the light weight of fiber optic current sensors, combined with their ability to measure strong current without conducting it, make them a prominent solution to measure current due to lightning during plane flights. They are a cost-efficient and safe technology that could replace most common solutions that measure the magnetic field and then require subsequent integration. Laboratory testing have confirmed the advantages of this technology. [2]

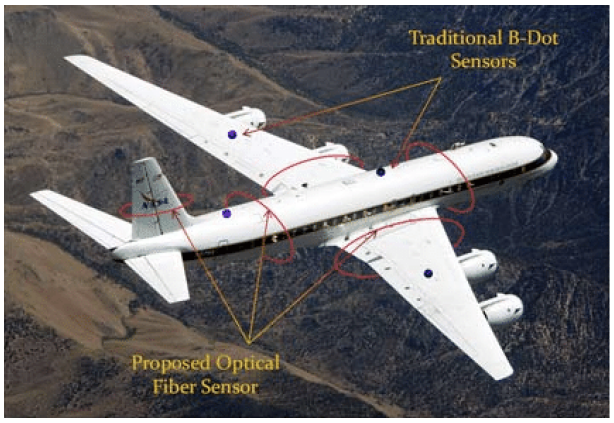


Fig. 10: Optical fiber current sensors as they would be implemented on a plane [2]

## 5.2 Faraday effect in plasmonic and magnetic materials

### 5.2.1 Plasmonic materials and magnetic materials

Plasmonic materials, such as gold and silver, exhibit a strong interaction between light and free electrons, plasmons, on their surface. The collective oscillation of the conduction electrons (Figure 11, [17]) when excited with light at specific wavelengths, leads to significantly higher scattering and absorption of light compared to particles of different materials. Plasmon surface resonance is shown to enhance the Faraday effect, contributing to a more pronounced rotation in the polarization of light.

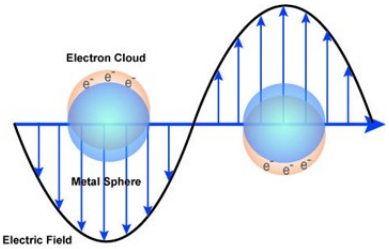


Fig. 11: Oscillation of plasmons

As discussed in section 2, in magnetic materials, the magnetic moments of the material's atoms and ions, in the presence of an external magnetic field, cause the plane of polarization of the light to rotate.

### 5.2.2 Composite nanostructure made of both plasmonic and magnetic material

By creating a composite nanostructure consisting of a magnetic maghemite nanoparticle ($\gamma$-$Fe_2O_3$) coated with a plasmonic gold (Au) shell, the effect of the Faraday rotation can be enhanced [18].

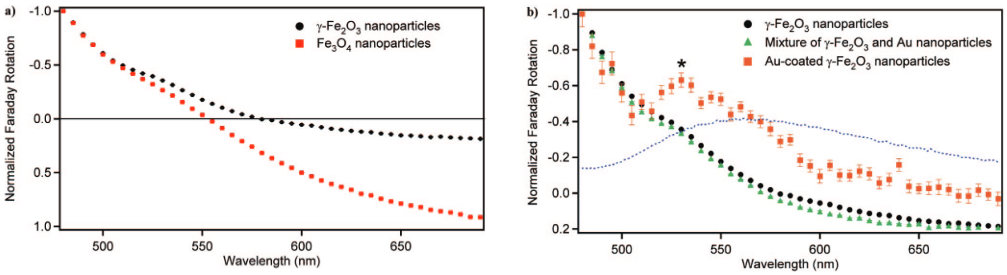


Fig. 12: (a) Normalized Faraday rotation spectra of $\gamma$-$Fe_2O_3$ nanoparticles and $Fe_3O_4$ nanoparticles. (b) Normalized Faraday rotation spectra of $\gamma$-$Fe_2O_3$ nanoparticles, gold-coated $\gamma$-$Fe_2O_3$ nanoparticles, and a mixture of $\gamma - Fe_2O_3$ and gold nanoparticles.The absorbance spectrum showing the plasmon resonance band of the gold-coated $\gamma$-$Fe_2O_3$ nanoparticles is indicated by the dotted blue curve [18].

By performing Faraday rotation measurements for different magnetic maghemite nanoparticle both with and without gold coating, the gold-coated-$\gamma$-$Fe_2O_3$ nanoparticles showed a similar rotation spectrum to the uncoated particles, with the exception of a sharp peak at around 530 nm (Figure 12 [18]). The fact that the mixture of $\gamma$-$Fe_2O_3$ nanoparticles and gold nanospheres doesn't show a peak in that wavelength demonstates that it is a consequence of the close coupling between the gold shell and the $\gamma$-$Fe_2O_3$ nanoparticle.

This peak corresponds to an intrinsic electronic transition in the maghemite nanoparticles and its magnitude is mainly due to the spectral overlap of the surface plasmon resonance in the gold (peak at around 520nm, depending on the size of the nanoparticles [8]) with the electronic transition in maghemite (peak at around 550 nm [19]).

#### 5.2.3 Applications of these nanostructures

While surface plasmon resonance is already exploited to improve efficiency of solar cells, improve optical fibers and for biosensors, the great enhancement of the Faraday effect in these composite nanostructures may enable design of nanostructures for remote sensing and imaging of magnetic fields and for miniaturized magneto-optical devices.

### 5.3 The Faraday effect in the ionosphere

One of the natural occurrences of the Faraday effect in nature is the rotation of the polarization of radio waves in the ionosphere. The ionosphere is the final layer of the Earth's atmosphere, located between 80 and 600 kilometers above the Earth's surface (Figure 13). Extreme Ultraviolet and X-ray solar radiation bombards the upper layer of Earth's atmosphere, which ionizes molecules and atoms creating a layer of electrons [20]. The ionosphere and the Earth's magnetic field can influence the propagation and attenuation of electromagnetic waves, including inducing Faraday rotations on radio and microwaves.

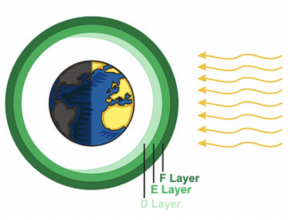


Fig. 13: Layers of the ionosphere [21]

The ionosphere has significant consequences on satellite and telecommunications. In particular, the total electron content (TEC) accumulated along a mobile-satellite service transmission path through the ionosphere is affected by Faraday rotation, and thus can cause time delays in the arrival of signals [22].

We will now discuss a specific instance of the Faraday rotation and its effect on satellites, in particular its effect on L-Band (Wavelength of 24 cm) on Interferometric and Polarimeteric Synthetic Aperture Radar (SAR) Data, discussed in Ringot's article [7]. Interferometric data from satellites helps produce accurate topographical maps, while polarimetric data analyzes the polarization of electromagnetic radiation. This is particularly relevant for monitoring various geophysical parameters at the Earth's surface, such as vegetation biomass and soil moisture.

Let us assume that the ionosphere has a constant vertical and horizontal electron density profile, and a constant magnetic field direction along an entire transmission path. Then the Faraday rotation angle $\beta$ can be expressed as:

$$\beta = 2.1610^{-13}\text{TEC}\,\text{B}\,\lambda^2\cos(\theta)[23] \tag{10}$$

- $\beta$ Faraday Rotation angle in radians
- TEC in electrons per $m^2$: electron content of the slab of ionosphere
- B Earth's magnetic field (T)
- $\lambda$ Radar wavelength in meters
- $\theta$ Angle between B and radar illumination in radians

Using data from the shuttle imaging radar C (SIR-C) and the Japanese Earth Resources Satellite (JERS-1), the study simulates the effects of Faraday rotation on SAR data. The instrument of the SIR-C satllite records the complete scattering matrix **S** by combining transmit and receiving signals at horizontal (H) and vertical (V) linear polarization where:

$$\mathbf{S} = \begin{pmatrix} S_{HH} & S_{VH} \\ S_{HV} & S_{VV} \end{pmatrix}$$

Each coefficient $S_{XY}$ represents complex scattering amplitudes at X-polarization transmit and Y-polarization receive. If the signal is affected by Faraday rotation then **S** is modified according to:

$$\mathbf{M{=}FSF} \tag{11}$$

with **F** the Faraday rotation matrix:

$$\begin{pmatrix} \cos(\beta) & -\sin(\beta) \\ \sin(\beta) & \cos(\beta) \end{pmatrix}$$

Using these matrix equations, simulations were run to see how the Faraday effect affects temporal coherence and phase coherence. The study finds that phase coherence is reduced up to 33% when the rotation angle $\beta$ changes between successive data acquisitions. Notably large rotation angles $\beta$ heavily impair topographical mapping, and hence Faraday rotation must be taken into consideration for satellites intended for this use.

## 6 Conclusions

By modeling the Faraday effect, we gained a comprehensive understanding of how this phenomenon arises from Maxwell's equations in matter. We were able to effectively recover the expression for the angle of rotation of polarization of a plane wave both through the Lorentz model approach, as well as by looking at indices of refraction. Our simulations demonstrated that the rotation of the polarization angle is directly proportional to both the distance traveled and the magnetic field's intensity. In addition we learned how to solve Maxwell's equations numerically by approximating partial derivatives, and how to incorporate current sources in our code. We were able to discover the implementation of absorbing boundary conditions, allowing the wave to exit the medium without reflection at its boundary.

A first limitation of the approach that we took would be that we had to set an unphysically high magnetic field to compensate for the short length of the medium that we could simulate (given that our step size was the order of nanometers and for computation times we had to limit the number of steps). However, this could be easily solved by increasing the number of steps using a higher performance device. Furthermore, to simplify our model we made the assumption of considering a plasmonic material ($\omega_0 \approx 0$). We could extend our model by considering $\omega_0 \neq 0$. This would add a term $+\omega_0^2 \vec{P}$ in the first order differential equation for the current density $\vec{J}$. Since $\frac{\partial \vec{P}}{\partial t} = \vec{J}$, we would obtain the time-evolution of $\vec{J}$ by solving the system of the two first order differential equations for $\vec{J}$, using the same method as the one we already implemented.

There are several ways in which we can continue to further the research that we have conducted thus far and advance what we have seen. First we can improve the numerical methods that we have used, such as implementing an adaptive mesh refinement (AMR) to our FDTD maxwell solver [24]. AMR was developed for parabolic partial differential equations and uses a hierarchical mesh. The advantage of this would be that the spatial-resolution of the grid that we implement could be adjusted, so that more computational resources can be directed to areas of the grid where they are most needed, such as at boundaries or where there are high field gradients. This could make our scheme more efficient and save memory. Furthermore, we could improve upon the absorbing boundary conditions and implement a perfectly matched layer (PML) which is often used in FDTD simulations designed to absorb incident light with minimal reflections [25]. PML boundaries are basically implemented as an absorbing material

that is also impedance matched to the surrounding materials, in order to minimize reflections. This could further enhance our simulation and better our results.

Additionally, to continue to increase the realism of our model we could introduce materials with dispersion and non-linearity, to better understand their influence on the Faraday rotation and achieve more accurate simulations. It could also be useful to try and verify our simulated results experimentally. An experimental apparatus for this could include a laser diode incident on a glass rod of known length, suspended in the middle of a solenoid producing a known constant magnetic field [26]. Measuring the produced light through a photo diode could then result in a measurement of the total Faraday rotation, and could be compared with our simulated results to see if our simulation and theory predicts what we intend to see accurately.

# A Appendix

## A.1 Derivation of the phase velocities 2

This section provides the calculations to obtain the wave numbers and phase velocities of the right-handed and left-handed circular polarizations.

From the differential equation satisfied by the position of the electron, of charge $-e = -1.6 \times 10^{-19}$C and mass $m_e = 9.1 \times 10^{-31}$kg in a non-relativistic case

$$\ddot{\vec{\mathrm{r}}} + \gamma \dot{\vec{\mathrm{r}}} + \omega_0^2 \vec{\mathrm{r}} = \frac{-e}{m_e}\vec{E} + \frac{-e}{m_e}\vec{v_e} \times \vec{B_0}$$

By considering:

- An electromagnetic plane wave propagating in the $x$ direction: $\vec{E}(x, y, z, t) = Re(\vec{E_0}e^{i(kx-wt)})$
- The external magnetic field along the direction of propagation of the wave $\vec{B_0} = B_0\vec{e_x}$
- The collision time is $\tau$ is large enough to neglect the contribution of the $\gamma\dot{\vec{\mathrm{r}}}$ with respect to the other terms in the equation.

By using an ansatz $\vec{r} = Re(y_0 e^{-i\omega t}\vec{e_y} + z_0 e^{-i\omega t}\vec{e_z})$ we get:

$$\begin{pmatrix} (\omega_0^2 - \omega^2) & -i\omega\Omega \\ i\omega\Omega & (\omega_0^2 - \omega^2) \end{pmatrix} \begin{pmatrix} y \\ z \end{pmatrix} = \frac{-e}{m_e} \begin{pmatrix} E_y \\ E_z \end{pmatrix}$$

where we have used the cyclotron frequency $\Omega = \frac{eB_0}{m_e}$. By inverting the matrix we get

$$\begin{pmatrix} y \\ z \end{pmatrix} = \frac{-e}{m_e} \frac{1}{(\omega_0^2 - \omega^2)^2 - (\omega\Omega)^2} \begin{pmatrix} \omega_0^2 - \omega^2 & i\omega\Omega \\ -i\omega\Omega & \omega_0^2 - \omega^2 \end{pmatrix} \begin{pmatrix} E_y \\ E_z \end{pmatrix}$$

From this, introducing $n$, the electron density, we find the current density

$$\vec{j} = \begin{pmatrix} j_y \\ j_z \end{pmatrix} = -ne\vec{v} = \frac{-ne^2 i\omega}{m_e((\omega_0^2 - \omega^2)^2 - (\omega\Omega)^2)} \begin{pmatrix} \omega_0^2 - \omega^2 & i\omega\Omega \\ -i\omega\Omega & \omega_0^2 - \omega^2 \end{pmatrix} \begin{pmatrix} E_y \\ E_z \end{pmatrix} \tag{12}$$

Using the plasma frequency $\omega_p^2 = \frac{ne^2}{m_e\epsilon_0}$, we find:

$$\vec{j} = \begin{pmatrix} j_y \\ j_z \end{pmatrix} = \frac{-i\omega\epsilon_0\omega_p^2}{(\omega_0^2-\omega^2)^2-(\omega\Omega)^2} \begin{pmatrix} \omega_0^2-\omega^2 & i\omega\Omega \\ -i\omega\Omega & \omega_0^2-\omega^2 \end{pmatrix} \begin{pmatrix} E_y \\ E_z \end{pmatrix} =: [\sigma] \begin{pmatrix} E_y \\ E_z \end{pmatrix} \tag{13}$$

Then, from Maxwell's equations we derive the propagation equation

$$\Delta\vec{E} - \mu_0\epsilon_0\frac{\partial^2\vec{E}}{\partial t^2} = \mu_0\frac{\partial\vec{j}}{\partial t}$$

Using an ansatz $\vec{E}(x,y,z,t) = \vec{E_0}e^{i(kx-wt)}$ with $\vec{E_0} = E_{0y}\vec{e_y} + E_{0z}\vec{e_z}$ and equation 12, we get:

$$-k^2 \begin{pmatrix} E_y \\ E_z \end{pmatrix} - \mu_0\epsilon_0(-\omega^2) \begin{pmatrix} E_y \\ E_z \end{pmatrix} = -i\omega\mu_0[\sigma] \begin{pmatrix} E_y \\ E_z \end{pmatrix}$$

$$(-k^2\mathbb{1} + \frac{\omega^2}{c^2}\mathbb{1} + i\omega\mu_0[\sigma]) \begin{pmatrix} E_y \\ E_z \end{pmatrix} = 0$$

We are not interested in the trivial solution $\vec{E} = \vec{0}$ and therefore obtain the equation:

$$(-k^2\mathbb{1} + \frac{\omega^2}{c^2}\mathbb{1} + i\omega\mu_0[\sigma]) = 0$$

For this equation to hold, the eigenvalues of the following matrix $M$ must be equal to 0.

$$M := -k^2\mathbb{1} + \frac{\omega^2}{c^2}\mathbb{1} + i\omega\mu_0[\sigma]$$

We observe that we only need to diagonalize $[\sigma]$ for the matrix $M$ to be diagonal.

We get:

$$M = \begin{pmatrix} -k^2 + \frac{\omega^2}{c^2}(1 + \frac{\omega_p^2}{(\omega_0^2-\omega^2)^2-(\omega\Omega)^2}(\omega_0^2-\omega^2+\omega\Omega)) & 0 \\ 0 & -k^2 + \frac{\omega^2}{c^2}(1 + \frac{\omega_p^2}{(\omega_0^2-\omega^2)^2-(\omega\Omega)^2}(\omega_0^2-\omega^2-\omega\Omega)) \end{pmatrix}$$

For both eigenvalues to be zero, we have

$$\begin{cases} -k^2 + \frac{\omega^2}{c^2}(1 + \frac{\omega_p^2}{(\omega_0^2-\omega^2)^2-(\omega\Omega)^2}(\omega_0^2-\omega^2+\omega\Omega)) = 0 \\ -k^2 + \frac{\omega^2}{c^2}(1 + \frac{\omega_p^2}{(\omega_0^2-\omega^2)^2-(\omega\Omega)^2}(\omega_0^2-\omega^2-\omega\Omega)) = 0 \end{cases}$$

from which we find the two dispersion relations:

$$\begin{cases} k_1^2 = \frac{\omega^2}{c^2}(1 + \frac{\omega_p^2}{(\omega_0^2-\omega^2)-(\omega\Omega)}) \\ k_2^2 = \frac{\omega^2}{c^2}(1 + \frac{\omega_p^2}{(\omega_0^2-\omega^2)+(\omega\Omega)}) \end{cases}$$

noting that the first relation is valid for fields of the form $\begin{pmatrix} E_y \\ -iE_z \end{pmatrix}$ (right-handed circular polarization) and the second dispersion relation is valid for fields of the form $\begin{pmatrix} E_y \\ iE_z \end{pmatrix}$ (left-handed circular polarizations).

From there we find that right-handed and left-handed circular polarized wave propagate respectively at velocity $v_R$ and $v_L$:

$$\begin{cases} v_R = \dfrac{c}{\sqrt{1+\frac{\omega_p^2}{(\omega_0^2-\omega^2)-(\omega\Omega)}}} \\ v_L = \dfrac{c}{\sqrt{1+\frac{\omega_p^2}{(\omega_0^2-\omega^2)+(\omega\Omega)}}} \end{cases}$$

### A.2 Derivation of the Verdet constant $V$

We have found that the rotation angle writes as $= \frac{k_R-k_L}{2}$ with:

$$\begin{cases} k_R^2 = \dfrac{\omega^2}{c^2}(1+\dfrac{\omega_p^2}{(\omega_0^2-\omega^2)-(\omega\Omega)}) \\ k_L^2 = \dfrac{\omega^2}{c^2}(1+\dfrac{\omega_p^2}{(\omega_0^2-\omega^2)+(\omega\Omega)}) \end{cases}$$

We consider that $\omega$ is far enough from resonance frequency such that $\frac{\omega\Omega}{\omega_0^2-\omega^2} \ll 1$ and rewrite:

$$\begin{cases} k_R^2 = \dfrac{\omega^2}{c^2}(1+\dfrac{\omega_p^2}{\omega_0^2-\omega^2}(\dfrac{1}{1-\frac{\omega\Omega}{\omega_0^2-\omega^2}})) \\ k_L^2 = \dfrac{\omega^2}{c^2}(1+\dfrac{\omega_p^2}{\omega_0^2-\omega^2}(\dfrac{1}{1+\frac{\omega\Omega}{\omega_0^2-\omega^2}})) \end{cases}$$

Then by using Taylor expansion in the first order, we find:

$$\frac{1}{1-\frac{\omega\Omega}{\omega_0^2-\omega^2}} \approx 1+\frac{\omega\Omega}{\omega_0^2-\omega^2}$$

and

$$\frac{1}{1+\frac{\omega\Omega}{\omega_0^2-\omega^2}} \approx 1-\frac{\omega\Omega}{\omega_0^2-\omega^2}$$

Giving:

$$\begin{cases} k_R^2 = \dfrac{\omega^2}{c^2}(1+\dfrac{\omega_p^2}{\omega_0^2-\omega^2}(1+\dfrac{\omega\Omega}{\omega_0^2-\omega^2})) \\ k_L^2 = \dfrac{\omega^2}{c^2}(1+\dfrac{\omega_p^2}{\omega_0^2-\omega^2}(1-\dfrac{\omega\Omega}{\omega_0^2-\omega^2})) \end{cases}$$

Then

$$k_R^2 - k_L^2 = 2\frac{\omega^2}{c^2}\frac{\omega\Omega\omega_p^2}{(\omega_0^2-\omega^2)^2}$$

Next, since $\frac{\omega\Omega}{\omega_0^2-\omega^2} \ll 1$, we find $k_R \approx k_L \approx \frac{\omega}{c}(1+\frac{\omega_p^2}{\omega_0^2-\omega^2})^{\frac{1}{2}}$ Finally, we get

$$k_R - k_L = \frac{k_R^2-k_L^2}{k_R+k_L} = \frac{\omega^2}{c}\frac{\omega_p^2\Omega}{(\omega_0^2-\omega^2)^2(1+\frac{\omega_p^2}{\omega_0^2-\omega^2})^{\frac{1}{2}}}$$

Recalling that $\Omega = \frac{eB_0}{m_e}$, we recover the linear dependence of the rotation angle on the external magnetic field:

$$\beta = VB_0L$$

where $V$ is the Verdet constant and is identified as: $V = \frac{k_R^2-k_L^2}{k_R+k_L} = \frac{\omega^2 e}{2m_e c}\frac{\omega_p^2}{(\omega_0^2-\omega^2)^2(1+\frac{\omega_p^2}{\omega_0^2-\omega^2})^{\frac{1}{2}}}$. Under the assumption that $\omega_0 \approx 0$, as it is the case in a plasmonic material, and as we considered in our simulation, and considering $\omega_p \ll \omega$, we can further simplify the expression of $V$: $V = \frac{e}{2m_e c}\frac{\omega_p^2}{\omega^2}$.

### A.3 Detail of the resolution of the time evolution for the current $J_+$ for section 3.2

This section provides the reader with the detailed steps for the resolution of the time evolution equation for $J_+ = J_y + iJ_z$, given by:

$$\frac{\partial J_+}{\partial t} + \Gamma J_+ = \epsilon_0 \omega_p^2 (E_y + iE_z) \tag{14}$$

**Step 1: Solve the associated homogeneous equation $\frac{\partial J_+}{\partial t} + \Gamma J_+ = 0$ (H)**

Integrating over time we find $J_{+,H} = Ce^{-\Gamma t}$ where C is an integration constant.

**Step 2: Find a particular solution for the full equation** We consider the ansatz: $J_{+,A}(t) = J(t)e^{-\Gamma t}$ for the time evolution equation of $J_+$ We have

$$\frac{\partial J_+}{\partial t} = \frac{\partial J}{\partial t} e^{-\Gamma t} - \Gamma J(t) e^{-\Gamma t}$$

. Then 14 becomes:

$$\frac{\partial J(t)}{\partial t} = \epsilon_0 \omega_p^2 [(E_y(t) + iE_z(t)] e^{\Gamma t}$$

Integrating with respect to time we find

$$J(t) = J(t_0) + \epsilon_0 \omega_p^2 \int_{t_0}^{t} [(E_y(t') + iE_z(t')] e^{\Gamma t'} dt'$$

We consider the particular solution with $J(t_0) = 0$, yielding

$$J_{+,A}(t) = \epsilon_0 \omega_p^2 \int_{t_0}^{t} [(E_y(t') + iE_z(t')] e^{\Gamma (t'-t)} dt'$$

**Step 3: we find the solution to the full equation**

Any solution to the equation 14 writes as the sum of the solution to the homogeneous equation $(H)$ and of a particular solution. Hence we find:

$$J_+(t) = J_{+,H}(t) + J_{+,A}(t) = Ce^{-\Gamma t} + \epsilon_0 \omega_p^2 \int_{t_0}^{t} [(E_y(t') + iE_z(t')] e^{\Gamma (t'-t)} dt'$$

With the initial condition $Ce^{-\Gamma t_0} = J_+(t_0)$, we find

$$J_+(t) = J_+(t_0) e^{-\Gamma (t-t_0)} + \epsilon_0 \omega_p^2 \int_{t_0}^{t} [(E_y(t') + iE_z(t')] e^{\Gamma (t'-t)} dt'$$

### A.4 Fiber Optics Current Sensors: detail of the derivation to obtain $S = \sin(2\beta)$

We consider unpolarized light (of intensity $I_0$) that goes through a first linear polarizer $P_1$, then through the Faraday sensing fibers, and finally is split by a prism in two beams of orthogonal polarization. This is equivalent to considering that half of the beam goes through a polarizer $P_2^+$ oriented at +45° compared to the polarization axis of $P_1$ and the other half through $P_2^-$ oriented at -45°.

Applying Malus' law, for unpolarized light, we find that the intensity after $P_1$ is

$$I_1 = I_0 \frac{1}{2\pi} \int_0^{2\pi} \cos^2 \theta d\theta = \frac{I_0}{2}$$

After going through the Faraday sensing element, the light's linear polarization is shifted by angle $\beta$ compared to the polarization axis of $P_1$.
Applying Malus' law again, we find that after $P_2^+$ and $P_2^-$ the intensities are respectively:

$$I_2^+ = I_1 \cos^2(\frac{\pi}{4} - \beta)$$

$$I_2^- = I_1 \cos^2(\frac{\pi}{4} + \beta)$$

Expanding the squares and using trigonometric identities we find

$$I_2^+ = \frac{I_0}{2} * \frac{1}{2}(1 + \sin(2\beta))$$

$$I_2^- = \frac{I_0}{2} * \frac{1}{2}(1 - sin(2\beta))$$

Then the function S is

$$S = \frac{I_2^+ - I_2^-}{I_2^+ + I_2^+} = \sin(2\beta)$$

## Contributions

All group members worked on the different parts of the projects, with weekly team meetings, with and without Professor Arnaud Couairon, to discuss the different steps of the project. Nevertheless, the different group members each had a specific focus. Sascha Rosenbaum led the research on the relevance and the applications of the Faraday effect. Clémence Moullet focused on the theoretical approach and explaining of the phenomenon. Emma Sampietro concentrated on the simulation and analysis of the result. Finally, each member studied in depth an application of the Faraday effect.

## Additional Resources

For more information and to access the project's source code, visit the GitHub repository:
`https://github.com/EmmaSampietro/Faraday-effect-simulator.git`

## References

1. T. E. of Encyclopaedia Britannica, "Faraday effect," *Encyclopaedia Britannica*, 2024, accessed: 2024-05-21. [Online]. Available: https://www.britannica.com/science/Faraday-effect
2. T. X. Nguyen, J. J. Ely, G. N. Szatkowski, C. T. Mata, A. G. Mata, and G. P. Snyder, "Lightning current measurement with fiber-optic sensor," in *2014 International Conference on Lightning Protection (ICLP)*, 2014, pp. 1424–1431.
3. A. Optics, "Faraday effect and optical isolator," *Ansys Optics Learning Center*, 2024, accessed: 2024-05-21. [Online]. Available: https://optics.ansys.com/hc/en-us/articles/360042274774-Faraday-effect-and-optical-isolator
4. M. S. Sodha and S. P. Sinha, "Experimental observation of faraday effect in a plasma and its theoretical interpretation," *International Journal of Electromagnetics and Applications*, vol. 7, no. 1, pp. 17–21, 2017, accessed: 2024-05-21. [Online]. Available: http://article.sapub.org/10.5923.j.ijea.20170701.03.html

5. S. K. Coffey and T. C. Grabowski, "High current sensing through faraday rotation of polarized light of varying wavelengths in fibers," June 2017, conference presentation at the 2017 IEEE International Pulsed Power Conference, Brighton, United Kingdom, June 18-22, 2017. Accessed: 2024-05-21. [Online]. Available: https://www.osti.gov/servlets/purl/1455380
6. B. Gaensler. (2024) Cosmic magnetism. Dunlap Institute for Astronomy and Astrophysics, University of Toronto. [Online]. Available: https://www.dunlap.utoronto.ca/observational-research/galaxy-formation-and-evolution/cosmic-magnetism/
7. E. J. M. Rignot, "Effect of faraday rotation on l-band interferometric and polarimetric synthetic-aperture radar data," *IEEE Transactions on Geoscience and Remote Sensing*, vol. 38, no. 1, p. 383, January 2000.
8. X. Huang and M. A. El-Sayed, "Gold nanoparticles: Optical properties and implementations in cancer diagnosis and photothermal therapy," *Journal of Advanced Research*, 2024. [Online]. Available: https://www.researchgate.net/publication/240931213_Gold_nanoparticles_Optical_properties_and_implementations_in_cancer_diagnosis_and_photothermal_therapy
9. M. E. Sharifabad, R. Soucaille, X. Wang, M. Rotherham, T. Loughran, J. Everett, D. Cabrera, Y. Yang, R. Hicken, and N. Telling, "Optical microscopy using the faraday effect reveals in situ magnetization dynamics of magnetic nanoparticles in biological samples," *ACS Nano*, vol. 18, no. 7, pp. 5297–5310, 2024, pMID: 38315113. [Online]. Available: https://doi.org/10.1021/acsnano.3c08955
10. J. B. Schneider, *Understanding the Finite-Difference Time-Domain Method.* Pullman, WA: School of Electrical Engineering and Computer Science, Washington State University, Aug. 2023.
11. D. B. Davidson, "Formulation of 1d fdtd," 2020, accessed: 2024-05-23. [Online]. Available: https://empossible.net/wp-content/uploads/2020/01/Lecture-Formulation-of-1D-FDTD.pdf
12. E. Hecht, *Optics, Global Edition.* Pearson, n.d., references on p.82 and p.382.
13. A. Kumar, J. Dash, and D. Sarkar, 05 2022, the Yee-grid template was taken from that reference and edited according to our model.
14. H. T. Taub and E. G. Stephen. (2020) Lecture: Formulation of 1d fdtd. [Online]. Available: https://empossible.net/wp-content/uploads/2020/01/Lecture-Formulation-of-1D-FDTD.pdf
15. W. Hua and J. He. Magneto-optic over-current detection with null optical tuning. [Online]. Available: https://www.researchgate.net/publication/279847047_Magneto-Optic_Over-Current_Detection_with_Null_Optical_Tuning
16. T. G. Nguyen, "A review on problems and counter-measures in design and fabrication of opical current sensors," 11 2016.
17. NanoComposix. (2024) The science of plasmonics. [Online]. Available: https://nanocomposix.com/pages/the-science-of-plasmonics
18. A. Cohen, "Surface plasmon resonance enhanced magneto-optics (supremo): Faraday rotation enhancement in gold-coated iron oxide nanocrystals," *Nano Letters*, vol. 9, pp. 1644–1650, 2009.
19. S. Mizuno and H. Yao, "Absorption properties of maghemite," *Journal of Magnetism and Magnetic Materials*, 2024. [Online]. Available: https://www.sciencedirect.com/science/article/pii/S0304885320323568
20. National Oceanic and Atmospheric Administration (NOAA). (2024) Ionosphere. [Online]. Available: https://www.swpc.noaa.gov/phenomena/ionosphere
21. ——. (2024) Ionosphere - the maximum usable frequency (muf). [Online]. Available: https://www.noaa.gov/jetstream/ionosphere-max
22. International Telecommunication Union (ITU), "ITU-R recommendation P.531-6: Propagation data and prediction methods for the planning of terrestrial line-of-sight systems," International Telecommunication

Union (ITU), Tech. Rep., 2001. [Online]. Available: https://www.itu.int/dms_pubrec/itu-r/rec/p/R-REC-P.531-6-200102-S!!PDF-E.pdf

23. K. Davies, *Ionospheric Radio Propagation*. Washington, DC: United States Dept. Commerce, 1965.
24. Y. Liu and C. Sarris, "Amr-fdtd: a dynamically adaptive mesh refinement scheme for the finite-difference time-domain technique," in *2005 IEEE Antennas and Propagation Society International Symposium*, vol. 1A, 2005, pp. 134–137 Vol. 1A.
25. A. Optics, "Pml boundary conditions in fdtd and mode," 2023, accessed: 2024-05-23. [Online]. Available: https://optics.ansys.com/hc/en-us/articles/360034382674-PML-boundary-conditions-in-FDTD-and-MODE
26. D. Whiteson, "Faraday's law lab report," Department of Physics Astronomy University of California, Irvine, 2024, https://www.physics.uci.edu/~advanlab/faraday.pdf.